Development of a Lensless Radiomicroscope for Cellular-Resolution Radionuclide Imaging

Justin S. Klein, Tae Jin Kim, and Guillem Pratx

Department of Radiation Oncology, Stanford University, Stanford, California

The action of radiopharmaceuticals takes place at the level of cells. However, existing radionuclide assays can only measure uptake in bulk or in small populations of single cells. This potentially hinders the development of effective radiopharmaceuticals for disease detection, staging, and treatment. **Methods:** We have developed a new imaging modality, the lensless radiomicroscope (LRM), for in vitro, cellular-resolution imaging of β- and α-emitting radionuclides. The palm-sized instrument is constructed from off-the-shelf parts for a total cost of less than $100, about 500 times less than the radioluminescence microscope, its closest equivalent. The instrument images radiopharmaceuticals by direct detection of ionizing charged particles via a consumer-grade complementary metal-oxide semiconductor detector. **Results:** The LRM can simultaneously image more than 5,000 cells within its 1 cm^2 field of view, a 100-times increase over state-of-the-art technology. It has spatial resolution of 5 μm for brightfield imaging and 30 μm for ^{18}F positron imaging. We used the LRM to quantify ^{18}F-FDG uptake in MDA-MB-231 breast cancer cells 72 h after radiation treatment. Cells receiving 3 Gy were 3 times larger (mean = 3,116 μm^2) than their untreated counterparts (mean = 940 μm^2) but had 2 times less ^{18}F-FDG per area (mean = 217 Bq/mm^2), a finding in agreement with the clinical use of this tracer to monitor response. Additionally, the LRM was used to dynamically image the uptake of ^{18}F-FDG by live cancer cells, and thus measure their avidity for glucose. **Conclusion:** The LRM is a high-resolution, large-field-of-view, and cost-effective approach to image radiotracer uptake with single-cell resolution in vitro.

Key Words: radionuclide imaging; in vitro assays; ^{18}F-FDG; CMOS detector

The past decade has witnessed a significant increase in the number of radiopharmaceuticals approved for diagnostic and therapeutic use in humans. To receive such approval, these radiopharmaceuticals have undergone rigorous evaluation and characterization, including preclinical and clinical studies. During the early phase of this process, in vitro data are often generated to identify and validate promising leads. In addition, existing radiopharmaceuticals continue to be studied even well after they have been approved for human use (*1–3*). However, most in vitro cell studies are limited in their ability to resolve the action of the radiopharmaceuticals at the level of individual cells. Most existing assays can only measure the aggregated behavior of millions of cells, complicating efforts to study specific cells of interest within heterogeneous populations (*4*).

Radioluminescence microscopy (RLM), a technique for in vitro radionuclide imaging, was previously developed to address this need. The method allows dynamic imaging of live cells over a 1 mm^2 field of view, equating to approximately 50–100 cells simultaneously. RLM consists of a high-sensitivity camera coupled to a microscope objective that images a thin (typically 100–500 μm) scintillator placed above or below a culture monolayer (*2*). By imaging β-particle scintillation tracks and applying a reconstruction algorithm (*5*), high-resolution and quantitative measurements of single cells are achievable (*6*). RLM has been used to study metabolism with ^{18}F-FDG (*7*) and cell proliferation with ^{18}F-fluorothymidine (*1*) in cell monolayers. The method can also be applied to image 3-dimensional (3D)–cultured cells including engineered tumor-stroma models (*8*) and patient-derived tumor organoids (*9*).

However, the small field of view of RLM presents a challenge for biologic experiments, requiring repeated acquisitions to attain statistical significance, since it is too small to measure sufficient numbers of cells and collect information on rare cell populations, such as tumor progenitor cells (*10*).

Additionally, it should be noted that building a RLM and successfully executing experiments requires significant technical skill and, to the best of our knowledge, only a few laboratories have adopted this technique. The cost of the necessary equipment is also significant, hindering dissemination and commercialization of the technique to more sites.

Here, we report the development of a lensless radiomicroscope (LRM) for in vitro, cellular-resolution radionuclide imaging of large cell populations. Unlike RLM, the LRM uses neither a scintillator nor a microscope objective. Instead, its design is based on the concept of lensless imaging (Fig. 1A), which was previously demonstrated for imaging cell samples using cell phone cameras or inexpensive photosensor arrays (*11*). This new microscope can image brightfield and radionuclide uptake of >5,000 cells, a 100× increase over RLM, with spatial resolution of 30 μm for radionuclide imaging and 5 μm for brightfield imaging. Additionally, the LRM is a simple and compact device built from inexpensive, readily available consumer electronics. With a total price tag of under $100 USD, it costs approximately 500× less than RLM, its predecessor, yet it can acquire radionuclide and brightfield images with similar performance.

To demonstrate the capabilities of this new instrument, we have used the LRM to image the dynamic uptake of ^{18}F-FDG by MDA-MB-231 breast cancer cells. Additionally, we have demonstrated that it is sensitive to α-particles, enabling its application for imaging therapeutic radiopharmaceuticals in vitro.
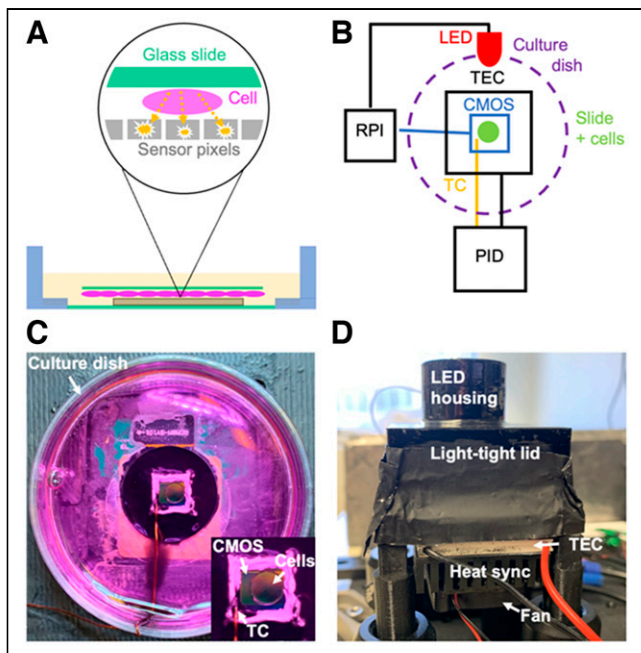
FIGURE 1. Conceptual, physical, and schematic diagram of the LRM. (A) Cells are grown on a glass slide and treated with α- or β-emitting radiopharmaceuticals. The slide is inverted and placed in direct contact with a CMOS imaging sensor. Emitted particles deposit energy in adjacent CMOS pixels, producing a detectable electronic signal. (B) The LRM consists of an imaging sensor (CMOS) that is read out through a compact Raspberry Pi computer (RPI). For live-cell imaging, sensor temperature is regulated by a proportional-integral-derivative (PID) controller connected to a thermocouple (TC) and thermoelectric cooler (TEC). The computer is also connected to an LED, which can be switched on for brightfield imaging. (C) The β-microscope imaging chamber, filled with medium. (D) Light-tight β-microscope enclosure. The LED used for brightfield imaging is housed in the upper cylinder. Attached to the bottom of the enclosure are the thermoelectric cooler, heat sync and fan.

MATERIALS AND METHODS

β-Microscope Design

The β-microscope comprises a light-tight imaging chamber with a removable lid made from 3D-printed parts (Fig. 1D). Inside the imaging chamber (Fig. 1C) is a pixelated Sony IMX219 complementary metal-oxide semiconductor (CMOS) imaging detector (Pi camera V2.1; Raspberry Pi Foundation, U.K.) integrated into a 35-mm-diameter cell-imaging dish (Cellvis). The imager has $3{,}280 \times 2{,}464$ square pixels, each 1.12 μm in size, and a total active area of 3.79×2.69 mm. The whole imaging dish is easily removable via a J2 FPC connector on the bottom of the dish that mates with the microscope's imaging chamber.

The imaging detector is connected to the camera serial interface of a compact computer (Raspberry Pi Model 3B+; Raspberry Pi Foundation, U.K.). Custom, Python-based software (Python Software Foundation) controls the instrument for brightfield and radionuclide imaging. Microscope software and computer-aided design models are available in our public Git repository: https://github.com/jstklein/lrm. Temperature is controlled during cell imaging via a thermoelectric cooler that is coupled to the underside of the Pi camera circuit board. The cooler is controlled by a proportional-integral-derivative controller that is connected to a thermocouple bonded to the CMOS surface (Fig. 1C).

The light-tight enclosure features a 30-mm-long tube and aperture-masked red (~640 nm) light-emitting diode (LED) that is driven by a 5 V input/ouput port on the Raspberry Pi computer through a 1 kΩ current-limit resistor (Fig. 1D). The LED provides semicollimated light for lensless brightfield imaging. We tested other visible wavelength LEDs (green, white) and found all yielded qualitatively similar results and the red LED was arbitrarily chosen. Given the proximity of the cells to the CMOS sensor, brightfield images can be obtained directly from the sensor without any additional reconstruction.

Imaging Dish Construction

The lens assembly of the Pi camera was removed, and the CMOS detector was carefully extracted from the camera housing. Exposed gold bondwires were protected from the aqueous cell culture environment using a waterproof silicon sealant (Marine Adhesive Sealant 5200FC; 3M). The detector was then glued into the hole at the bottom of the plastic imaging dish using 832HD epoxy (MG Chemicals). Finally, a glass coverslip was glued behind the detector, sealing the bottom of the imaging chamber.

Cell Imaging

Cells were grown on glass coverslips that had been prepared for cell culture (*12*) and subsequently treated with fibronectin (Sigma Aldrich) to improve biocompatibility and facilitate cell attachment. For all imaging experiments, MDA-MB-231 breast cancer cells were grown on round glass coverslips and submerged upside down into the imaging chamber, in direct contact with the CMOS detector. During imaging, the proportional-integral-derivative controller is set to hold the temperature of the cells and medium to 37°C. Without active temperature control, the CMOS imager will exceed physiologic temperatures during operation and potentially interfere with normal cellular processes.

For static images, which capture total uptake at a single time point, cells were incubated in radiopharmaceutical, washed, and then imaged. For dynamic images, which capture the process of radiopharmaceutical transport and accumulation, the radiopharmaceutical was added directly to the imaging chamber and an image time series was captured immediately thereafter to visualize its uptake.

MDA-MB-231 cells (American Type Culture Collection) were cultured in Dulbecco modified eagle medium (DMEM) (catalog no. 11995-065; Thermo Fisher Scientific) supplemented with 10% fetal bovine serum (catalog no. F-0500-A; Atlas Biologicals) and 1% penicillin/streptomycin (cat. no. 15140122; Thermo Fisher Scientific) and incubated at 37°C in a 5% CO_2 environment.

Brightfield images were acquired using autoexposure mode at the maximum resolution of $3{,}280 \times 2{,}464$ pixels. Raw RGB images were converted to gray scale and stored as 16-bit JPEG2000 images.

To demonstrate the ability of the microscope to image cell staining, some MDA-MB-231 cells were additionally fixed and stained with crystal violet, first by being rinsed with phosphate-buffered saline, then by being incubated in 5% w/w crystal violet in 6% v/v glutaraldehyde (Sigma-Aldrich), and finally by being rinsed with tap water.

β- and α-images were acquired with the following settings: $3{,}280 \times 2{,}464$ pixels, 10-s exposure duration and analog gain of 2.5. A lower threshold of 3 camera counts was applied to each 10-s exposure to remove camera noise. Multiple thresholded exposures were summed in memory to produce output images with effective integration times ranging from approximately 1 to 10 min, depending on the experiment. No other image processing or filtering was performed. Image data were stored as a lossless lz4-compressed 16-bit image matrix. Image data and metadata were combined into a Python data structure, serialized using the Python Pickle format, then saved to file.

α-Imaging

α-emission from a 370-Bq ^{210}Po needle source (United Nuclear Scientific LLC) was imaged by placing the active tip directly on the microscope's CMOS surface. Three 5-min α-images were recorded and summed together. A brightfield image of the needle source was also recorded.

Physical Characterization

β-imaging resolution was assessed by applying the Fourier ring correlation method (13) to a representative image of ^{18}F-FDG uptake by cancer cells. Briefly, 2 images of the same cell population were generated, each constructed from half of the acquired frames. The method estimates the cross-correlation between the 2 images in the spatial frequency domain along concentric rings. A deterministic threshold of 1/7 is then used to yield a quantitative estimate of the spatial resolution of the imager.

In addition, brightfield resolution was characterized by imaging 1-μm amine-modified monodispersed superparamagnetic beads (Mono-Mag Amine Beads; Ocean NanoTech). The beads were diluted in ethanol and dried onto the surface of a glass microscope coverslip that was imaged using the brightfield mode of the β-microscope. Resolution was measured from the full width at half maximum of a line profile drawn across a single bead in the brightfield image.

Camera Calibration

A flatfield image was captured by illuminating the imaging sensor with uniform white light. This image was used to compute a per-pixel correction factor that was applied to images generated by the instrument. This correction factor accounts for any nonuniformities in the imaging sensor and lens-related calibration factors built into the proprietary camera firmware.

A calibration factor to convert camera units into ^{18}F activity was determined as follows. A drop of ^{18}F-FDG was dried on a glass slide, and activity was measured in a dose calibrator to be 108 kBq. The slide was imaged 397 min (~3.6 half-lives) later using the LRM, after it had decayed to 8.9 kBq. This low activity level was used to prevent camera saturation. A region of interest (ROI) was measured around the dried ^{18}F-FDG droplet. The camera calibration factor was computed as $\frac{\text{ROI counts (camera units)} \times \text{pixel area (mm}^2/\text{px)}}{\text{ROI activity (Bq)} \times \text{total imaging time (s)}}$, where pixel area $= 1.25 \times 10^{-6}$ mm^2/px (based on CMOS pixel pitch).

RESULTS

Characterization

Supplemental Figure 1 (supplemental materials are available at http://jnm.snmjournals.org) shows a time-integrated β-microscope image of a dried 8.9-kBq ^{18}F-FDG droplet on a glass slide. The final camera calibration factor was computed using the equation shown above and average measurements from 3 independent, 50 s β-images. The measurements were ROI counts = 422,845,211, ROI activity = 8.9 kBq, and total imaging time = 50 s. The final calibration factor was $840 \frac{\text{camera units} \times \text{mm}^2}{\text{Bq} \times \text{s} \times \text{px}}$, where px is pixels. When divided into ^{18}F β-images on a per-pixel basis, the calibration factor yields quantitative images in units of Bq/mm^2.

Brightfield resolution was 5.1 μm, based on the full width at half maximum of a 1-μm polystyrene sphere (Fig. 2A). The inset image in Figure 2 shows a line profile drawn across the sphere (dashed blacked line), and arrows show full width at half maximum. β-resolution was 30 μm, based on Fourier ring correlation analysis of ^{18}F-FDG β-images of MDA-MB-231 cells (Fig. 2B). This resolution is equivalent to that of RLM and largely determined by the source-detector distance and the physics of positron transport (6).

Brightfield Imaging

To demonstrate the timelapse capabilities of the LRM and the ability of cells to remain viable over prolonged imaging
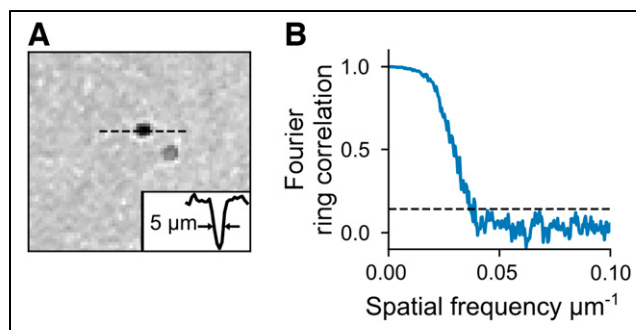

FIGURE 2. LRM physical characterization and calibration. (A) Brightfield image of 1-μm polystyrene sphere with inset line profile showing full width at half maximum. (B) Fourier ring correlation analysis plot showing spatial resolution of RLM.

experiments, MDA-MB-231 cells were grown on a glass slide, then imaged in brightfield mode every 5 min, for 10 h (Supplemental Fig. 2A). Cell migration could be readily observed in a recorded video of the acquisition (Supplemental Video 1), and no adverse effects were detected.

Additionally, the microscope is capable of imaging fixed and stained cells. Supplemental Figure 2A shows enlarged senescent MDA-MB-231 cells after irradiation with 8 Gy (225 kVp x-ray) and subsequent fixing and staining with crystal violet in glutaraldehyde. The use of a stain induces a visible darkening of the cells in the brightfield images.

^{18}F-FDG β-Microscope Imaging

We first demonstrate the LRM technique by imaging ^{18}F-FDG uptake in MDA-MB-231 breast cancer cells (Fig. 3). The β-image is the sum of 13 images, each acquired as a 5-min exposure (65 min total imaging time). The merged image shows that ^{18}F-FDG uptake can be localized to individual cells and matches the brightfield image. Because of the proximity of the cells to the detector, the outline of the cells is clearly resolved, with only overlap between adjacent cells. About 50 cells are shown in the cropped field of view and range in activity from 0 Bq/mm^2 up to 1,800 Bq/mm^2, indicating a wide range of metabolic activity in this population. Healthier-looking cells (larger, attached, dividing) appear to be more metabolically active than unhealthy ones (detached, granular, shriveled). The images also confirm that background signal is very low in areas where cells are not present, even for extended imaging experiments.
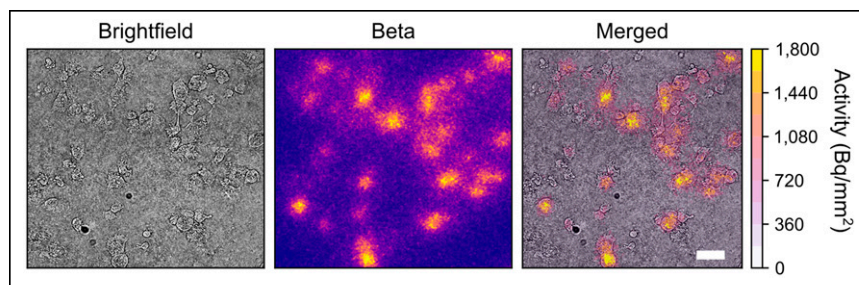

FIGURE 3. High-resolution β-imaging of ^{18}F-FDG in breast cancer cells. MDA-MB-231 cells were imaged using brightfield and β-modes. Images are cropped to 600 × 600 μm from the full 3.7 × 2.8 mm field of view. Total imaging time for β-imaging was 65 min. Scale bar is 50 μm.
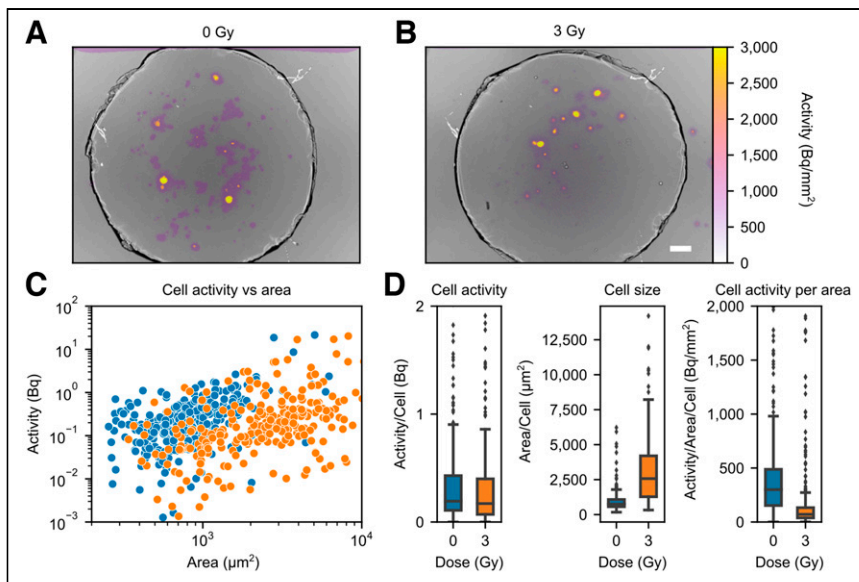
FIGURE 4. ^{18}F-FDG β-imaging of breast cancer cells treated with radiation. β-images of cells receiving 0 Gy (A) and 3 Gy (B). Scale bar is 200 μm. (C) Scatter plot of activity vs. area for treated and untreated cells. (D) Bar graphs of activity per cell, cell size, and cell activity per area.

^{18}F-FDG Imaging of Radiation-Treated Breast Cancer Cells

Figure 4 demonstrates that LRM can be used to determine the response of MDA-MB-231 cells to radiation therapy on the basis of ^{18}F-FDG uptake. Cells were irradiated with 0 and 3 Gy of 225 kVp x-ray 3 d before image acquisition using the LRM.

To quantify the images, ROIs were drawn around cells, and area and activity were measured. Figure 4C shows activity versus area for all cells in the experiment. Data represent ROIs measured from 4 β-images with total integration times of 75 min (0-Gy experiment) and 45, 60, or 105 min (3-Gy experiment).

Figure 4D shows aggregated measurements from cell ROIs. Cells receiving 0 Gy ($n = 301$) had significantly smaller area (mean = 940 μm^2) but overall greater activity per area (mean = 445 Bq/mm^2). Cells receiving 3 Gy ($n = 260$) had larger area (mean = 3116 μm^2), but less activity per area (mean = 217 Bq/mm^2). All results were statistically significant ($P < 0.01$) per Welch's t test. Both groups had similar activity per cell (0-Gy mean = 0.50 Bq; 3-Gy mean = 0.67 Bq; $P > 0.01$).

Dynamic ^{18}F-FDG β-Microscope Imaging

Figure 5 demonstrates dynamic imaging of ^{18}F-FDG uptake by MDA-MB-231 cells over a 190 min period. LRM images were acquired every 10 min, resulting in 19 frames, and the corresponding time–activity curves were computed on the basis of user-defined circular ROIs (Fig. 5B). For this study, ^{18}F-FDG (5 MBq/mL) in DMEM was added to the imaging chamber immediately before imaging the dynamic uptake of the tracer by the cells. The average ^{18}F-FDG distribution over the entire study period is shown in Figure 5B, along with the ROIs that were used. The time–activity curves for the cells were corrected by subtracting the background signal.
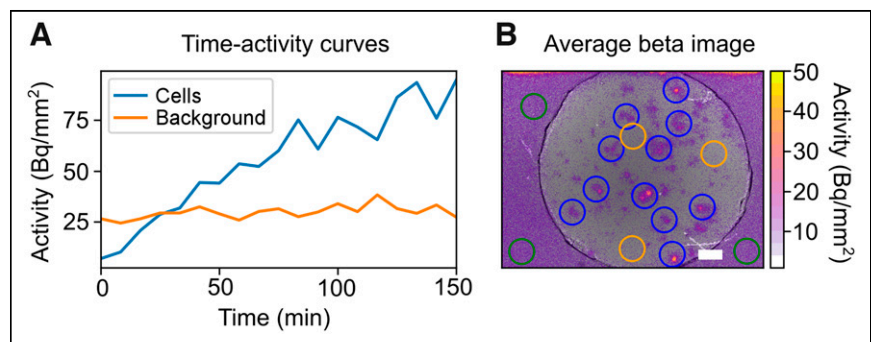
The β-image was merged with the gray scale brightfield image, and ROIs were drawn over clusters of cells (blue) and empty background regions (orange). The image shows regions of significant focal uptake, corresponding to dense clusters of cells. Background signal was significantly lower under the cover glass than outside of it because of the lower volume and shielding by the cover glass.

Time–activity curves of cell and background ROIs (Fig. 5A) show ^{18}F-FDG uptake as a function of time. These curves have been corrected for radioactive decay and drift in detector gain by normalizing them using the background signal outside the circular cover glass region. A movie of ^{18}F-FDG uptake has been included as Supplemental Video 2.

α-Particle Imaging

Figure 6 shows α- and brightfield images of a ^{210}Po needle source. The needle appears as a long dark shadow in the brightfield image. The α-image is the sum of 3 5-min acquisitions. Compared with β-particles, α-particles produce an intense and focal signal on the detector. The merged image shows that the α-signal is readily localized to the needle source.

DISCUSSION

This study presents a novel lensless radiomicroscope that can image commonly used radiotracers at single-cell resolution in 2-dimensional cell cultures. The instrument is compact and inexpensive, yet it can image samples with >1 cm^2 field of view and 30-μm spatial resolution. The microscope is capable of prolonged, timelapse brightfield in vitro imaging of stained or unstained cells (Supplemental Fig. 2, Supplemental Video 1), and β- (Figs. 3, 4, and 5) or α- (Fig. 6) imaging.

Compared with other solid-state radiation detectors, such as, for instance, a position-sensitive avalanche photodiode (14), a lensless CMOS detector can also be used for imaging cells in brightfield mode, providing images of both the cells and the distribution of the radiotracer. These capabilities could potentially be embedded

FIGURE 5. Dynamic ^{18}F-FDG imaging of cells. (A) Time–activity curves measured from cell and background ROIs. (B) Cumulative uptake of ^{18}F-FDG by MDA-MB-231 cells, with ROIs shown for cells (blue) and background (orange). Scale bar is 200 μm.
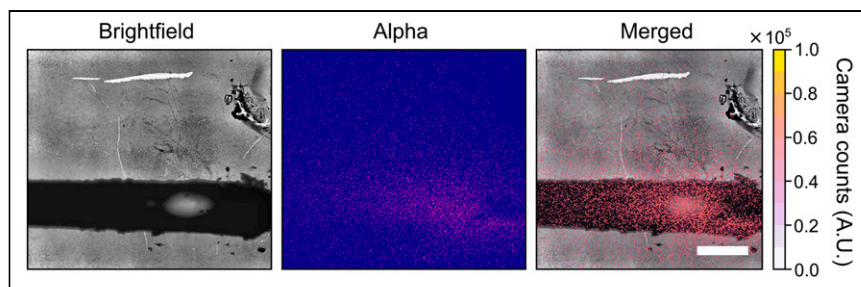
FIGURE 6. α-imaging of Po-210 needle source. The needle is visible as a dark shadow in the brightfield image. α-emission is readily localized to the needle source in the merged image. Scale bar is 500 μm.

within microfluidics devices for in vitro radiobiologic assays (*13*) or for quality control of radiotracer production (*15*). Additionally, the system is built from inexpensive consumer-grade components, including a Raspberry Pi minicomputer ($35), a CMOS camera ($25), a Peltier cooling system ($35), and a 3D printed housing (<$10). The system is therefore highly cost-effective compared with other previously developed imaging methods.

Figure 3 reveals static ^{18}F-FDG β-images of MDA-MB-231 cells and shows that the β-signal is easily localized to individual cells. The spatial resolution of ^{18}F images is estimated to be 30 μm, based on Fourier ring correlation analysis of the LRM images, which is sufficient in most cases to distinguish individual cells. This estimate, which is obtained through a computational method, is consistent with the fact that, in Figure 3, adjacent cells can be readily resolved. Spatial resolution for β-imaging is primarily determined by the physical travel of the positrons before reaching the sensor, regardless of the type and pixel size of the sensor used to detect the ionizing radiation. Thus, although the pixels are very small, the spatial resolution of the LRM is similar to that of other methods that rely on larger pixels, such as RLM (*6*). The use of CMOS devices with larger pixels could potentially allow improved signal to noise with no loss of resolution, however, the trend in consumer camera electronics is toward smaller form factors and pixels. Additionally, once calibrated, the LRM can be used to provide quantitative estimates of radioactivity distribution in cells. The calibration factor we have provided is relevant only for ^{18}F and the calibration procedure would have to be repeated if other isotopes were imaged.

To illustrate the capabilities of the microscope, we measured ^{18}F-FDG uptake in cells irradiated with 0 or 3 Gy of x-rays (Fig. 4). Radiation is often used as a treatment for solid tumors, with nearly 50% of all cancer patients receiving some form of radiation for their disease. ^{18}F-FDG PET is a common readout of treatment response, but the significance of the PET measurement is unclear because irradiated cells may remain metabolically active, even if they can no longer replicate. To investigate this question, measurements from more than 500 cells were made using the β-microscope in a single experiment. Three days after receiving 3 Gy of x-ray radiation, cells were on average 3 times larger (mean area = 3,116 μm^2) than their untreated counterparts but had half as much ^{18}F-FDG per area. The brightfield images also revealed that the cells treated with 3 Gy had enlarged nuclei, a common occurrence in radiation-treated cells that is due to the failure of these cells to advance through mitosis. The decreased ^{18}F-FDG concentration inside the cells suggests decreased metabolic activity, likely due to radiation-induced damage of the cell's metabolic machinery. Of note,

previous studies noted that cells that survived irradiation actually had higher ^{18}F-FDG uptake than control nonirradiated cells (*16,17*), based on bulk γ-counting measurements normalized by the number of viable cells. Our study found no substantial difference in uptake between nonirradiated and irradiated, but the difference may be due to the timing and methodology used for measuring this quantity.

Additionally, we demonstrated the feasibility of dynamic ^{18}F-FDG studies using the instrument (Fig. 6). Dynamic images were acquired every 10 min to yield aggregated time–activity curves that represent the active transport of the tracer by the cells. After decay correction, the measured background due to free ^{18}F-FDG in the culture medium was found to be constant over the course of the experiment. In contrast, the radioactive signal measured at the location of MDA-MB-231 cells rose over time at a nearly constant rate over the 2-h duration of the experiment. The imaged cells initially did not have any detectable radioactivity, but by the end of the experiment, they achieved radiotracer uptake equal to about 6 times the background concentration.

Finally, using a sealed ^{210}Po source, we demonstrated the ability of the LRM to image α-particles. This capability opens the door for imaging therapeutic α-emitting radionuclides, which are an important new class of therapy. The LRM in this context could be used to investigate the distribution of these agents at the level of individual cells in heterogeneous populations of cells and prevent the emergence of resistant subclones.

It should be noted that despite the impressive performance of this instrument, only minimal optimizations for image quality and sensitivity have been made thus far. There are likely significant gains to be had with further software optimization, alone. For example, in previous work, we found that signal-to-noise ratio could be significantly improved by processing the images in pulse-counting mode rather than integration mode (*5*). Similarly, the CMOS-based LRM could acquire large numbers of frames with short exposures to enumerate individual decay events.

Although the pixelated CMOS sensor provides many advantages for this application, a few limitations of the method should be highlighted. First, the 10 bit A/D converter limits the maximum signal to 1,024 camera units per pixel per frame. At a readout speed of 1 Hz, with ^{18}F, this would limit the maximum detectable activity to 10.8 Bq/px. Additionally, another limitation is that, unlike the previously developed RLM, the LRM lacks fluorescence capabilities. This capability could likely be enabled through harnessing built-in Bayer array or coating the CMOS pixels with a bandpass filter to obtain fluorescence images of cells in a lensless manner (*18*).

Finally, though we were able to reuse the same CMOS detector for many experiments, we expect that it will eventually degrade due to radiation damage. Given its relatively low cost, it is a consumable component of the microscope that can be regularly replaced.

CONCLUSION

The experiments shown here are a proof-of-concept for the LRM, a new imaging instrument capable of in vitro high-resolution imaging of β- and α-emitting radionuclides. This instrument is simpler and far less costly than current technology while offering an

unprecedently large 1 cm^2 field of view and 30-μm resolution. Our results demonstrate a variety of potential workflows that could foreseeably be used for radiopharmaceutical development, quality control, and cancer biology investigations. Because the LRM is low cost and constructed from readily available components, we anticipate that this new technology will make in vitro single-cell radionuclide imaging more accessible and enable new investigations in the biologic realm.

DISCLOSURE

KEY POINTS

QUESTION: Can a low-cost lensless radiomicroscope visualize cellular-level uptake of radionuclides?

PERTINENT FINDINGS: We have developed a low-cost imaging modality for in vitro imaging of α- and β-emitting radionuclides and imaged quantitative changes in cellular ^{18}F-FDG uptake after radiation treatment.

IMPLICATIONS FOR PATIENT CARE: The lensless radiomicroscope will aid in the development of effective radiopharmaceuticals by allowing study of their action at the cellular level.

REFERENCES

1. Sengupta D, Pratx G. Single-cell characterization of FLT uptake with radioluminescence microscopy. *J Nucl Med.* 2016;57:1136–1140.
2. Kim TJ, Türkcan S, Pratx G. Modular low-light microscope for imaging cellular bioluminescence and radioluminescence. *Nat Protoc.* 2017;12:1055–1076.
3. Liu Z, Lan X. Microfluidic radiobioassays: a radiometric detection tool for understanding cellular physiology and pharmacokinetics. *Lab Chip.* 2019;19:2315–2339.
4. Cherry SR, Sorenson JA, Phelps ME. What is nuclear medicine? In: *Physics in Nuclear Medicine.* Elsevier Health Sciences; 2012:1–6.
5. Pratx G, Chen K, Sun C, et al. High-resolution radioluminescence microscopy of ^{18}F-FDG uptake by reconstructing the β-Ionization track. *J Nucl Med.* 2013;54:1841–1846.
6. Wang Q, Sengupta D, Kim TJ, Pratx G. Performance evaluation of ^{18}F radioluminescence microscopy using computational simulation. *Med Phys.* 2017;44:1782–1795.
7. Pratx G, Chen K, Sun C, et al. Radioluminescence microscopy: measuring the heterogeneous uptake of radiotracers in single living cells. *PLoS One.* 2012;7:e46285.
8. Khan S, Kim S, Yang YP, Pratx G. High-resolution radioluminescence microscopy of FDG uptake in an engineered 3D tumor-stoma model. *Eur J Nucl Med Mol Imaging.* 2021;48:3400–3407.
9. Khan S, Shin JH, Ferri V, et al. High-resolution positron emission microscopy of patient-derived tumor organoids. *Nat Commun.* 2021;12:5883.
10. Reya T, Morrison SJ, Clarke MF, Weissman IL. Stem cells, cancer, and cancer stem cells. *Nature.* 2001;414:105–111.
11. Ozcan A, McLeod E. Lensless imaging and sensing. *Annu Rev Biomed Eng.* 2016;18:77–102.
12. Fischer AH, Jacobson KA, Rose J, Zeller R. Preparation of slides and coverslips for microscopy. *CSH Protoc.* 2008;2008:pdb.prot4988.
13. Kim TJ, Ha B, Bick AD, Kim M, Tang SKY, Pratx G. Microfluidics-coupled radioluminescence microscopy for in vitro radiotracer kinetic studies. *Anal Chem.* 2021;93:4425–4433.
14. Vu NT, Yu ZTF, Comin-Anduix B, et al. A beta-camera integrated with a microfluidic chip for radioassays based on real-time imaging of glycolysis in small cell populations. *J Nucl Med.* 2011;52:815–821.
15. Ha NS, Sadeghi S, van Dam RM. Recent progress toward microfluidic quality control testing of radiopharmaceuticals. *Micromachines (Basel).* 2017;8:337.
16. Higashi K, Clavo AC, Wahl RL. In Vitro Assessment of 2-fluoro-2-deoxy-D-glucose, L-methionine and thymidine as agents to monitor the early response of a human adenocarcinoma cell line to radiotherapy. *J Nucl Med.* 1993;34:773–779.
17. Senekowitsch-Schmidtke R, Matzen K, Truckenbrodt R, Mattes J, Heiss P, Schwaiger M. Tumor cell spheroids as a model for evaluation of metabolic changes after irradiation. *J Nucl Med.* 1998;39:1762–1768.
18. Kim M, Pan M, Gai Y, et al. Optofluidic ultrahigh-throughput detection of fluorescent drops. *Lab Chip.* 2015;15:1417–1423.